

Spin direction dependent quantum anomalous Hall effect in two-dimensional ferromagnetic materials

Yu-Xian Yang(杨宇贤) and Chang-Wen Zhang(张昌文)

Citation: Chin. Phys. B, 2024, 33 (**4**): 047101. DOI: 10.1088/1674-1056/ad1380
Journal homepage: http://cpb.iphy.ac.cn; http://iopscience.iop.org/cpb

What follows is a list of articles you may be interested in

Design of sign-reversible Berry phase effect in 2D magneto-valley material

Yue-Tong Han(韩曰通), Yu-Xian Yang(杨宇贤), Ping Li(李萍), and Chang-Wen Zhang(张昌文)
Chin. Phys. B, 2023, 32 (**9**): 097101. DOI: 10.1088/1674-1056/acd920

Topological properties of tetratomic Su-Schrieffer-Heeger chains with hierarchical long-range hopping

Guan-Qiang Li(李冠强), Bo-Han Wang(王博涵), Jing-Yu Tang(唐劲羽), Ping Peng(彭娉), and Liang-Wei Dong(董亮伟)
Chin. Phys. B, 2023, 32 (**7**): 077102. DOI: 10.1088/1674-1056/aca7ef

First-principles prediction of quantum anomalous Hall effect in two-dimensional Co_2Te lattice

Yuan-Shuo Liu(刘元硕), Hao Sun(孙浩), Chun-Sheng Hu(胡春生), Yun-Jing Wu(仵允京), and Chang-Wen Zhang(张昌文)
Chin. Phys. B, 2023, 32 (**2**): 027101. DOI: 10.1088/1674-1056/aca082

SU(3) spin-orbit coupled fermions in an optical lattice

Xiaofan Zhou(周晓凡), Gang Chen(陈刚), and Suo-Tang Jia(贾锁堂)
Chin. Phys. B, 2022, 31 (**1**): 017102. DOI: 10.1088/1674-1056/ac11dc

Control of topological phase transitions in Dirac semimetal films by exchange fields

Fei Yang(杨菲), Hai-Long Wang(王海龙), Hui Pan(潘晖)
Chin. Phys. B, 2017, 26 (**1**): 017102. DOI: 10.1088/1674-1056/26/1/017102

Spin direction dependent quantum anomalous Hall effect in two-dimensional ferromagnetic materials

Yu-Xian Yang(杨宇贤) and Chang-Wen Zhang(张昌文)†

School of Physics and Technology, University of Jinan, Jinan 250022, *China*

(Received 18 June 2023; revised manuscript received 7 December 2023; accepted manuscript online 8 December 2023)

We propose a scheme for realizing the spin direction-dependent quantum anomalous Hall effect (QAHE) driven by spin–orbit couplings (SOC) in two-dimensional (2D) materials. Based on the sp^3 tight-binding (TB) model, we find that these systems can exhibit a QAHE with out-of-plane and in-plane magnetization for the weak and strong SOC, respectively, in which the mechanism of quantum transition is mainly driven by the band inversion of $p_{x,y}/p_z$ orbitals. As a concrete example, based on first-principles calculations, we realize a real material of monolayer 1T-SnN_2/PbN_2 exhibiting the QAHE with in-plane/out-of-plane magnetization characterized by the nonzero Chern number C and topological edge states. These findings provide useful guidance for the pursuit of a spin direction-dependent QAHE and hence stimulate immediate experimental interest.

Keywords: topological phase transition, quantum anomalous Hall effect, first-principles calculations

PACS: 71.15.Mb, 73.43.–f, 73.63.–b **DOI:** 10.1088/1674-1056/ad1380

1. Introduction

Since the discovery of topological insulators,[1] the prediction and realization of new topological materials with exotic topological phases have drawn great fundamental and application research interest in condensed-matter physics and materials science.[2–6] Owing to the existence of dissipationless chiral edge states, the quantum anomalous Hall effect (QAHE) can be used to design low-power-consumption spintronic devices. This theoretical prediction has greatly stimulated the enthusiasm of researchers.[7–12]

Up to now, much effort has been made to find QAHE materials with a large band gap and high Curie temperature (TC), including surface functionalization on the buckled honeycomb lattices of silicene, germanene, and stanlene;[13,14] adsorbing diluted 3d, 4d, and 5d transition atoms on graphene;[8,15–17] construction of heterojunctions by depositing atomic layer elements on ferromagnetic insulators;[18–20] and applying the pure ferromagnetic semiconductor compound MX_3 without external field or additional doping.[21] Although there are a lot of theoretical predictions about the QAHE, its observation in experiments is rare. There are two essential ingredients for realizing the QAHE. One is ferromagnetism, which can be intrinsic magnetism of a material[22] or extrinsic magnetism induced by magnetic doping.[23] The other is spin–orbital coupling (SOC), which induces a nontrivial topological phase. Theoretically, plenty of materials have been predicted to exhibit the QAHE. Experimentally, however, only a minority of topological insulators are confirmed to exhibit the QAHE.[24,25] Recently, the quantized anomalous Hall conductance (AHC) plateau $\sigma_{xy} = e^2/h$ has been observed in $MnBi_2Te_4$ flakes.[26] Whether it can predict more QAHE is currently a hot topic.

In all these prior works, there is one default assumption, namely, that ferromagnetism must have an out-of-plane (OP) magnetization. This is similar to the quantum Hall effect that can only be observed in a perpendicular magnetic field.[27] Physically, the out-of-plane magnetization is only a sufficient, but not a necessary, condition for QAHE. Recently, researchers found that out-of-plane magnetization is not a necessary requirement; based on 2D point group symmetry analysis, in-plane (IP) magnetization can also induce a planar QAHE once all mirror symmetries are broken.[28–30] However, it is only recently that the QAHE with IP magnetization has been proposed in several models, e.g., magnetically doped Bi_2Te_3 thin films,[31] bulk hexagonal lattices,[29] and one real material of monolayer LaCl with a global band gap of 4 meV.[32] Therefore, there is a need to develop new theoretical models and search more candidate materials for accelerating the experimental confirmation of this new kind of topological phase.

Generally, a 2D lattice can sustain either one or both IP and OP mirror symmetry. Since IP magnetization can only break IP mirror symmetry, the possible 2D lattice to exhibit an IP QAHE must break OP mirror symmetry itself. Currently, all theoretical models for an IP QAHE are based on a buckling lattice, that is, the OP mirror symmetry is broken by the lattice configuration. Without losing the generality, different topological phases are determined by the direction of magnetization, mirror symmetry, and SOC. Based on sp^3 tight-binding (TB) models in a buckling lattice, we propose a different scheme for achieving an IP and an OP quantum anomalous Hall effect by regulating SOC strength, and apply this scheme to a two-dimensional metal nitride. Considering the successful prepa-

†Corresponding author. E-mail: ss_zhangchw@ujn.edu.cn

© 2024 Chinese Physical Society and IOP Publishing Ltd

ration of ReN_2 and MoN_2,[33,34] the successful preparation of metal nitrides is not out of reach, so it is meaningful to explore the QAHE in metal nitrides.

In this work, we systematically investigate monolayer SnN_2 and PbN_2 based on the first-principles calculations. Our results show that monolayers SnN_2/PbN_2 are stable. In the ground state, the monolayers have a half-metal band structure, and manifest a fully spin-polarized Weyl point at the Fermi level. They prefer an FM coupling with a high Curie temperature ($T_C = 768.7$ K), estimated by the spin-wave theory. We found that the SnN_2 monolayer with OP magnetization (MAE $= E_z - E_{x/y} = -0.080$ meV) is a QAH insulator and the PbN_2 monolayer with IP magnetization (MAE $= E_z - E_{x/y} =$ 0.065 meV) is a QAH insulator. More importantly, strain can adjust the direction of the easy magnetic axis in this system, i.e., IP magnetization and OP magnetization can be switched with each other.

2. Computational details

All structural and electronic properties are calculated using the Vienna *ab initio* simulation package based on spin-polarized density functional theory (DFT).[35] The exchange–correlation potential is described with the Perdew–Burke–Ernzerhof (PBE)[36] of the generalized gradient approximation (GGA).[37] The projected argument wave (PAW)[38] potential is used to describe the ion–electron potential. The energy cutoff of the plane wave is 500 eV. The Brillouin zone uses a convergent $11 \times 11 \times 1$ k mesh for structural relaxation and $33 \times 33 \times 1$ for electronic analysis. Both the atomic position and the lattice constant are relaxed until the force and energy converge to 0.001 eV/Å and 10^{-7} eV/atom. For XN_2, in order to avoid the interaction between adjacent layers, a vacuum space of about 20 Å is applied along the c direction. Based on the density of functional perturbation theory,[39] the phonon dispersion spectrum of XN_2 is calculated with the PHONOPY program,[40] and in this process, we use a $4 \times 4 \times 1$ supercell. *Ab initio* molecular dynamics (AIMD)[41] simulations are performed with a $3 \times 3 \times 1$ supercell at 300 K with a time step of 10 ps. The topological features of edge states were calculated by means of maximally localized Wannier functions implemented in the WANNIER90 package.[42]

3. Results and discussion

We first present our idea through the analysis of the TB model based on s, p_x, p_y, and p_z orbitals in point group, which is widely used to describe the physics of the hexagonal lattice. By employing a two-center approximation on the orthogonal basis,[30,43] the TB Hamiltonian takes the form

$$H = \sum_{i\alpha} \epsilon_\alpha c^\dagger_{i\alpha} c_{i\alpha} - \sum_{i\alpha,j\beta} t_{ij,\alpha\beta} c^\dagger_{i\alpha} c_{j\beta} + t_{\rm SO} \sum_{i\alpha,j\beta} c^\dagger_{i\alpha} \boldsymbol{l} \cdot \boldsymbol{s} c_{j,\beta} + \lambda \sum_{i\alpha} c^\dagger_{i\alpha} \hat{m} \cdot \boldsymbol{s} c_{i\alpha}, \quad (1)$$

where $c^\dagger_{i\alpha} = \left(c^\dagger_{i\alpha\uparrow}, c^\dagger_{i\alpha\downarrow}\right)$ represents the creation operator of an electron at the i-th atomic site with $\uparrow / \downarrow$ and α/β representing spin up/down channels and different orbitals, respectively. The first term represents the on-site energy due to C_{3z} symmetry; the on-site energies of p_x and p_y orbits are degenerate, while the p_z orbits are slightly different. The second term stands for the hopping energy up to next-nearest (NN) neighbor with an magnitude of $t_{ij,\alpha\beta}$, which is a function of the Slater–Koster parameters described in part I of the electronic support information (ESI). The third term represents the intra-atomic SOC with a strength of $t_{\rm so}$ with $\boldsymbol{s} = (s_x, s_y, s_z)$ and $\boldsymbol{l} = (l_x, l_y, l_z)$ being Pauli matrices and orbital-angular-momentum operators, which can be expressed as

$$H_{\rm SO} = t_{\rm SO} \begin{pmatrix} 0 & 0 & 0 & 0 \\ 0 & 0 & -{\rm i}s_z & {\rm i}s_y \\ 0 & {\rm i}s_z & 0 & -{\rm i}s_x \\ 0 & -{\rm i}s_y & {\rm i}s_x & 0 \end{pmatrix}. \quad (2)$$

The last term corresponds to an exchange coupling, J, between electron and magnetization which is defined as

$$(m_x, m_y, m_z) = \lambda \hat{m} = \lambda \left(\sin\theta\cos\phi, \sin\theta\sin\phi, \cos\theta\right), \quad (3)$$

where λ represents the magnetization strength, and polar angle θ and azimuthal angle φ are measured with respect to the z and x axes. The $\theta = 0$ indicates the magnetization direction is parallel to the z direction. When θ is equal to $\pi/2$, it means that the magnetization is located in the xy plane, and the specific orientation of magnetization is determined by the azimuthal angle φ.

To demonstrate the small band gap of the QAHE with Chern number $C = \pm 1$, we study the energy levels at the Γ point. For simplicity, we consider only $p_{x,y}$ and p_z orbitals. On the basis of $\left\{\left|p_x\right\rangle, \left|p_y\right\rangle, \left|p_z\right\rangle\right\} \otimes \{|\uparrow\rangle, |\downarrow\rangle\}$, the Hamiltonian around the Γ point for the band is reduced to

$$H_\Gamma = E_{\rm c} + \begin{pmatrix} \Delta\sigma_0 & -{\rm i}t_{\rm SO}\sigma_z & {\rm i}t_{\rm SO}\sigma_y & t_1\sigma_0 & 0 & 0 \\ {\rm i}t_{\rm SO}\sigma_z & \Delta\sigma_0 & -{\rm i}t_{\rm SO}\sigma_x & 0 & t_1\sigma_0 & 0 \\ -{\rm i}t_{\rm SO}\sigma_y & {\rm i}t_{\rm SO}\sigma_x & -\Delta\sigma_0 & 0 & 0 & t_2\sigma_0 \\ t_1\sigma_0 & 0 & 0 & \Delta\sigma_0 & -{\rm i}t_{\rm SO}\sigma_z & {\rm i}t_{\rm SO}\sigma_y \\ 0 & t_1\sigma_0 & 0 & {\rm i}t_{\rm SO}\sigma_z & \Delta\sigma_0 & -{\rm i}t_{\rm SO}\sigma_x \\ 0 & 0 & t_2\sigma_0 & -{\rm i}t_{\rm SO}\sigma_y & {\rm i}t_{\rm SO}\sigma_x & -\Delta\sigma_0 \end{pmatrix}, \quad (4)$$

where $\sigma_{x,y,z}$ are Pauli matrices and σ_0 is a 2×2 unit matrix. $E_c+\Delta=\epsilon_{px}+3\left(V'_{pp\pi}+V'_{pp\sigma}\right)$ and $E_c-\Delta=\epsilon_{pz}+6V'_{pp\pi}$ correspond, respectively, to the on-site energy of $p_{x,y}$ orbitals and p_z orbital with modifications from next-nearest-neighbor hopping. The interatomic hoppings for $p_{x,y}$ and p_z orbitals are t_1 and t_2, respectively.

Based on the Hamiltonian around the Γ point, band structures can be obtained, as shown in Fig. 1, in the presence of magnetization and a magnetization strength $\lambda=0.385$. We then apply the OP magnetization ($\theta=0$, $\varphi=\pi/2$), which meets the symmetry criteria of breaking all the mirror-reflection symmetries of the buckled honeycomb lattice.[28,29] In addition, we also consider the condition of IP ($\theta=\pi/2$, $\varphi=0$) magnetization. Figures 1(a)–1(c) and 1(e)–1(g) display, respectively, the band structures for OP and IP magnetization. For the same magnetization strength, whether it is OP magnetization or IP magnetization, we find that the increase of t_{so} shrinks the band gap and closes it at $t_{so}=0.28$ eV and $t_{so}=0.51$ eV for OP magnetization and IP magnetization, as indicated in Figs. 1(b) and 1(f). To realize the topological state, a nontrivial band inversion should be introduced. For the OP magnetization, with the increase in SOC strength, one can see that the gap can be first opened (Fig. 1(a), $t_{so}=0.12$ eV), then closed (Fig. 1(a), $t_{so}=0.28$ eV) and then reopened (Fig. 1(c), $t_{so}=0.35$ eV). Compared to OP magnetization, IP magnetization requires stronger SOC to realize band inversion. For the IP magnetization, we also see the same phenomenon, that the gap can be first opened (Fig. 1(e), $t_{so}=0.30$ eV), then closed (Fig. 1(f), $t_{so}=0.51$ eV) and then reopened (Fig. 1(g), $t_{so}=0.70$ eV).

The SOC-induced bandgap can be identified by Berry curvatures and Chern numbers given by[44,45]

$$\Omega(\boldsymbol{k})=\sum_n f_n\Omega_n(\boldsymbol{k}), \tag{5}$$

$$\Omega_n(\boldsymbol{k})=-\sum_{n'\neq n}2\mathrm{Im}\frac{\langle\psi_{nk}|v_x|\psi_{n'k}\rangle\langle\psi_{n'k}|v_y|\psi_{nk}\rangle}{(\varepsilon_{n'k}-\varepsilon_{nk})^2}, \tag{6}$$

where n is the band index, ψ_{nk} is the eigenstate of eigenvalue $E_{n\boldsymbol{k}}$ of band n, f_n is the Fermi distribution function, and $V_{x/y}$ is the velocity operator. By integrating $\Omega(\boldsymbol{k})$ over the first Brillouin zone (BZ), the Chern number (C) can be obtained from $C=\frac{1}{2\pi}\sum_n\int_{BZ}\mathrm{d}^2k\Omega_n(\boldsymbol{k})$. For both OP and IP magnetizations, as shown in Figs. 1(d) and 1(h), the nontrivial Berry curvature is mainly distributed around the Γ point. By integrating the Berry curvature, a nonzero Chern number $C=1$ is obtained, i.e., the SOC-induced bandgap is topologically nontrivial. This means that the band inversion between $p_{x,y}$ and p_z orbitals can also trigger the QAH phase regardless of OP and IP magnetizations.

Table 1. Calculated structure and magnetic properties of the XN_2 (X = Sn, Pb): lattice constant (a), X–N bond length (d_{X-N}), X–N–X bond angle (θ_{X-N-X}), formation energy (ΔE_f), exchange energy ($\Delta E_n=E_{NAFM}-E_{FM}$, $\Delta E_s=E_{SAFM}-E_{FM}$, $\Delta E_z=E_{ZAFM}-E_{FM}$) per unit cell, magnetic anisotropy energy.

Model	a (Å)	d_{X-N} (Å)	θ_{X-N-X} (°)	ΔE_f (eV)	ΔE_n (meV)	ΔE_s (meV)	ΔE_z (meV)	MAE (μeV)
SnN_2	3.43	2.24	79.8	−6.59	306.6	261.9	166.2	−80
PbN_2	3.54	2.31	79.7	−5.75	389.5	304.7	193.2	65

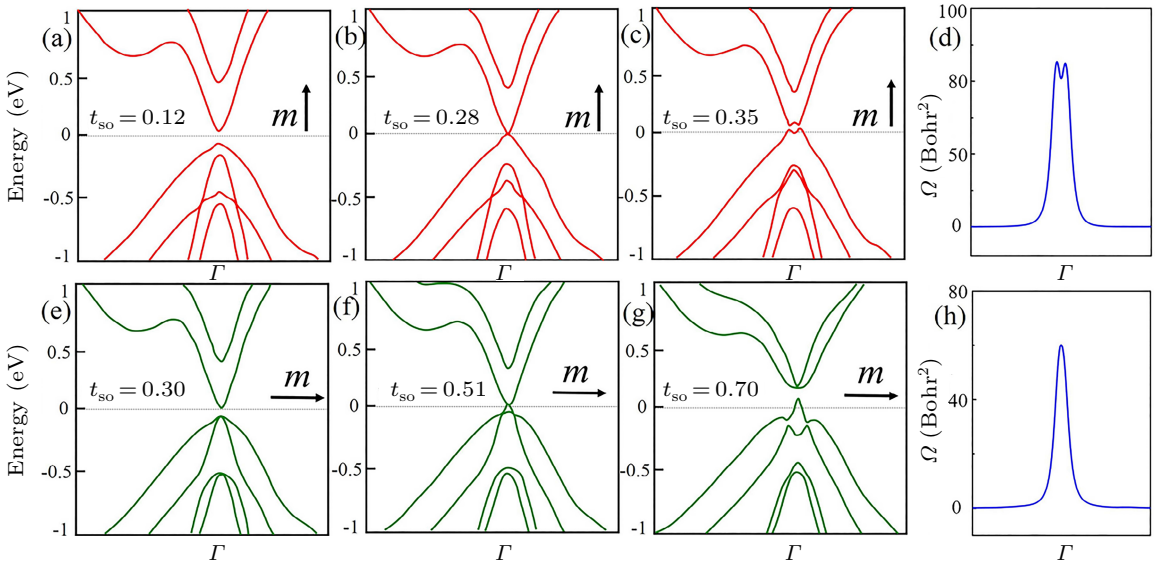


Fig. 1. (a)–(c) and (e)–(g) Corresponding 2D band structures along the high symmetry path around the Γ point for OP (red line) and IP (green line). Here, $\lambda=0.385$, t_{so} is 0.12 eV, 0.28 eV, 0.35 eV and 0.30 eV, 0.51 eV, 0.70 eV for panels (a)–(c) and (e)–(g), respectively. (d) and (h) Berry curvature distributions for band structures in panels (c) and (g).

The next key question is whether this TB model can be realized in real materials. Here, we investigate monolayer (ML) XN_2 (X = Sn, Pb) with a 1T structure as a representative example. The space group of XN_2 is $P\bar{3}m1$ (No. 164, D^3_{3d}), and its Wyckoff positions are X $(0,0,z)$ and N $(1/3,2/3,z)$. As shown in Fig. 2(b), the X atom is the inversion[46] center in the octahedral structure unit and the three N atoms in the upper layer will turn into the three N atoms in the lower layer under inversion. It has a hexagonal lattice with a 1T structural phase, where each X atom is bonded to six N atoms. The 1T structural phase has not only been realized in experiments, such as 1T-MoS_2,[47] 1T-TaS_2,[48] and 1T-$TiSe_2$,[49] but also widely applied for stable structural searches, such as transition-metal dihalides and transition-metal dinitrides,[50,51] indicating its rationality. The optimized lattice constant, X–N bond length, and N–N distance along the z-direction are shown in Table 1.

The structural stability is first examined by calculating the formation energy, $\Delta E_f = E(XN_2) - E(N_2) - E(X)$, where $E(XN_2)$ and $E(X)$ are the total energies of the XN_2 and X crystal, respectively, while $E(N_2)$ is the chemical potential of sulfur gas indicating its experimental feasibility. The obtained values, -6.59 eV and -5.75 eV per atom of SnN_2 and PbN_2, are lower than that of graphene (-8.66 eV per atom).[52] To further assess the stability of monolayer 1T-XN_2, we studied its lattice dynamics by calculating the phonon spectrum, which is shown in Fig. 2(b). It is free from imaginary frequency modes, which indicates that ML-SnN_2 and ML-PbN_2 are dynamically stable.

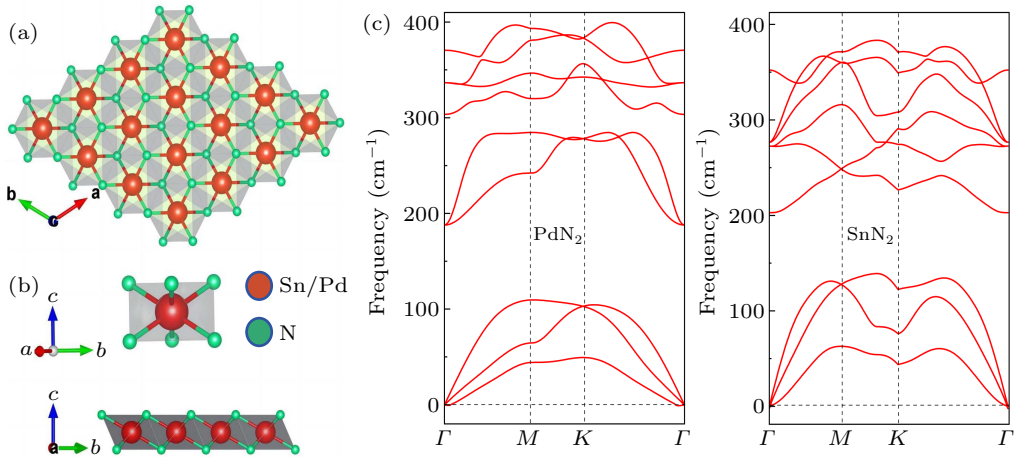


Fig. 2. (a) and (b) Schematic illustration of the XN_2 (X = Sn, Pb) crystal structure, which belongs to the space group $P\bar{3}m1$. (c) Phonon dispersion of the SnN_2 and PbN_2 monolayers.

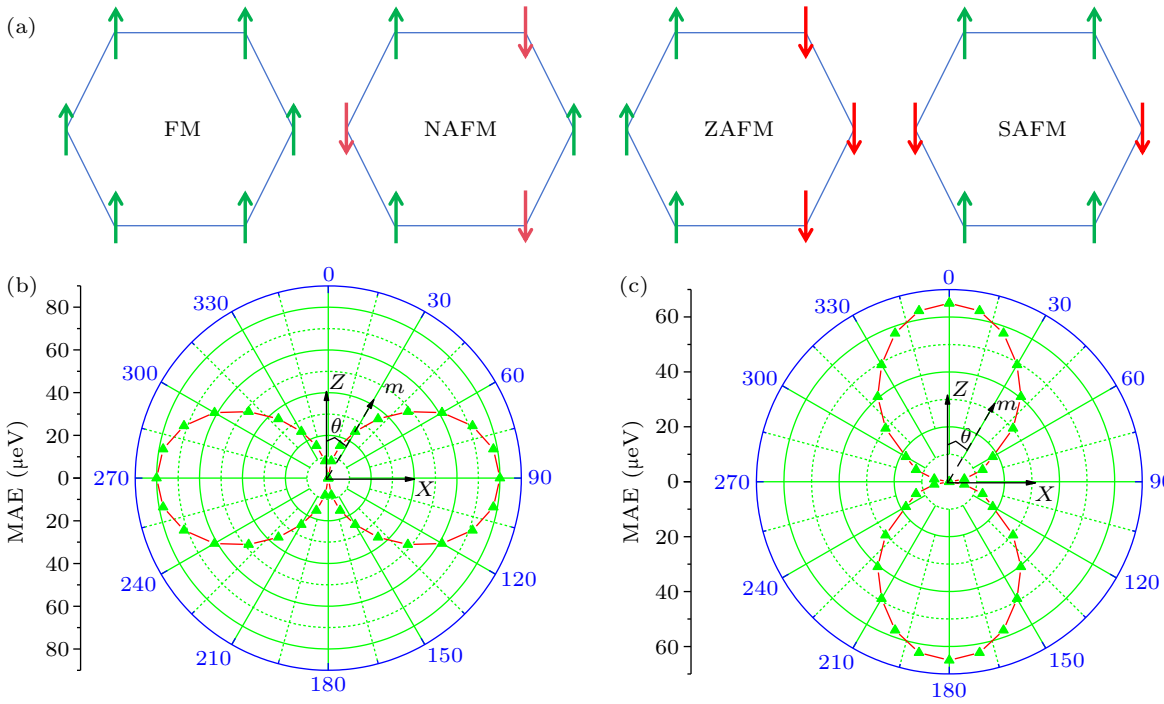


Fig. 3. (a) Possible magnetic configurations considered: ferromagnetic (FM), Néel antiferromagnetic (NAFM), stripe AFM (SAFM), and zigzag AFM (ZAFM). The magnetic moments are on the N sites forming a honeycomb lattice. (b)–(c) Magnetocrystalline anisotropy energy (MAE) for SnN_2 (b) and PbN_2 (c) by rotating the spin within z–x planes, respectively. The orange lines in the panel represent the fitted curves. $\mathrm{MAE}(\theta) = k_1 \times \cos^2\theta + k_2 \times \cos^4\theta$ and $\mathrm{MAE}(\varphi) = 0$, respectively.

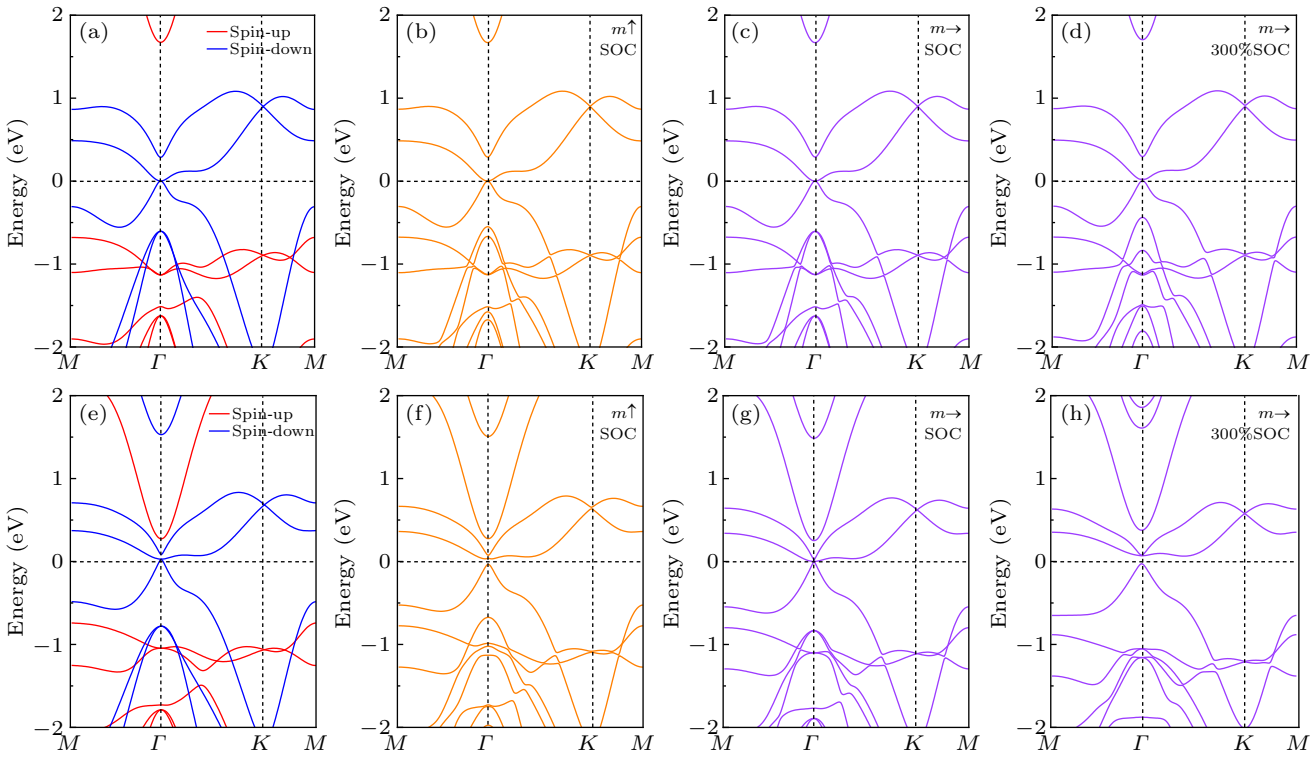


Fig. 4. Band structures of SnN_2 and PbN_2 lattices. (a), (c) and (b), (d) 2D SnN_2 and PbN_2 lattice without and with SOC for OP magnetization. (e), (g) and (f), (h) SnN_2 and PbN_2 with SOC for IP magnetization and artificially enhanced by 3 times in the calculation. Here, the red and blue lines denote spin-up and spin-down states, respectively.

Using high-throughput calculations, Liu *et al.* proposed a series of monolayers of a transition-metal dinitride, such as 1T-NbN_2 and 1T-TaN_2, which are ferromagnetic.[53] Due to the experimental feasibility and rich magnetic properties of these monolayers, it is thus an interesting question to search for more classes of stable monolayers of transition-metal dinitride. Now, we focus on the magnetic structures of ML-XN_2. To determine the magnetic ground state of XN_2, we consider several possible configurations, including FM, Néel antiferromagnetic (NAFM), stripe AFM (SAFM), and zigzag AFM (ZAFM), as shown in Fig. 3(a). The calculated results indicate that the FM state ($\Delta E_{\rm FM} = E_{\rm FM} - E_{\rm AFM}$) is lower than the NAFM, SAFM, and ZAFM states (detailed data can be seen in Table 1). In addition, we also check the spin configuration of the coplanar 120° AFM state, and find that the XN_2 monolayer prefers energetically the FM state ($\Delta E_{\rm FM} = 351.29$ meV/N). In the FM state, the XN_2 monolayer shows a large magnetic moment of 2 $\mu_{\rm B}$. We find that the magnetic moment of the XN_2 monolayer almost entirely originates from the N atoms. ESI-part II shows the spin density of the XN_2 monolayer, where the concentrated areas show the distribution of unpaired electrons. We can clearly observe that the unpaired electrons are mainly distributed around the N atoms, showing that the magnetism of the XN_2 monolayer comes from N rather than Sn or Pb. Based on the Mermin–Wagner theorem,[45] stable FM coupling is forbidden in the 2D isotropic Heisenberg model. However, finite magnetic anisotropy is able to protect long-range FM order.

Therefore, the stability of FM order in ML-XN_2 strongly correlates with its magnetic anisotropy energy (MAE), $\mathrm{MAE} = E_z - E_{x/y}$, which is defined as the energy difference between out-of-plane (OP) and in-plane (IP) magnetization. If the MAE is positive, it means that the energy along the IP direction is lower than the energy along the OP direction; thus, the MAE is along the IP direction. We found that the MAE of SnN_2 and PbN_2 are −80 μeV and 65 μeV, respectively, indicating that the magnetic easy axes are in the OP and IP directions, respectively. These finite values are larger than those of Ni, Fe and Co with MAE on the order of 1 μeV per unit cell.[55] According to the nearest-neighbor Heisenberg model, the Curie temperature can be estimated by $3k_{\rm B}T_{\rm c}/2 = (E_{\rm AFM} - E_{\rm FM})/N$, where $k_{\rm B}$ is the Boltzmann constant, N is the number of magnetic atoms in the supercell, and $E_{\rm AFM}$ and $E_{\rm FM}$ the total energies of AFM and FM configurations, respectively. We compared the total energies of XN_2 in FM and various AFM configurations (see Table 1), finding that $E_{\rm FM}$ is lower than $E_{\rm ZAFM}$ by 166.3 meV and 199.2 meV for ML-SnN_2 and PbN_2, which corresponds to Curie temperatures of 641.3 K and 768.7 K ($N = 2$). Therefore, ML-XN_2 can be ferromagnetic at room temperature.

Based on the FM ground state with 2 $\mu_{\rm B}$ magnetic moment, the electronic band structure of the ML-SnN_2 and ML-PbN_2 obtained by PBE calculation is shown in Figs. 4(a) and 4(b), where the red solid and blue dashed lines display spin-

up and spin-down channels, respectively. When considering the band structure without SOC, we found that the two spin channels have no degeneracy, forming a spontaneous spin polarization band structure. For the spin-up band, there is a large band gap of 0.93 eV and 2.40 eV for ML-SnN_2 and ML-PbN_2, respectively, showing the nature of an insulator. For the spin-down band, which shows spin gapless semiconductor (SGS) character, the valence band and the conduction band intersect at a single point at the Fermi level, thereby generating a degenerate point at Γ of the first BZ, as shown in Fig. 4. By using the Hall effect, one can easily separate spin-polarized carriers with a magnetic field applied perpendicular to the current direction, which is promising for designing field-induced self-spin filters.

Considering that the Sn and Pb atoms have a high magnetic quantum number, it is expected that SOC can also induce a large nontrivial band gap. Indeed, as shown in Figs. 4(c) and 4(d), we see a finite band gap opening at the Fermi level. The direct band gap at the Γ point is 9 meV and 67 meV for ML-SnN_2 and ML-PbN_2. We find that this is ten orders of magnitude higher than the experimental temperature at which the QAH effect is observed for a Cr-doped Bi_2Se_3 film.[24,56] Such a large band gap suggests that the PbN_2 monolayer might be a high-temperature QAH insulator. As is well known, the topological properties of the gap depend on the magnetization direction: when the magnetization direction is, for example, along the z axis, the magnetization direction breaks the vertical symmetry and induces a topologically nontrivial gap harboring a QAHE. An OP magnetization further results in a larger topologically nontrivial gap up to 67 meV of PbN_2 as shown in Fig. 4(d). In order to simulate band features of the TB model, we artificially increase the SOC strength by 3 times in DFT calculations, and plot the resulting band structures in Figs. 4(g) and 4(h). One can see that strong SOC can induce large nontrivial band gaps of 95 meV for PbN_2 and 12 meV for SnN_2.

Since ML-SnN_2 and ML-PbN_2 have a similar band structure, we will take PbN_2 as an example for further discussion. As shown in Fig. 5, taking PbN_2 as an example, we find that in the spin-down channel, the dominant contributions to the states near the Fermi level are obtained from the $p_{x,y}$ and p_z orbitals of N atoms, which drive $p_{x,y}$–p_z inversion, indicating that our TB model may be realized in this proposal. The projected band structures showed that the top valence band and bottom conduction bands are mainly contributed by N p_z and $p_{x,y}$ orbitals, respectively. We note that such combination of atomic orbitals just meets our TB model, indicating that any finite SOC can open a nontrivial bandgap, as confirmed by the detailed Chern number calculation later.

To confirm its nontrivial topological properties, we calculate its k-space Berry curvature, $\Omega(k)$, using the Kubo formula.[53,54] Figures 6(b) and 6(f) show the Berry curvature for the whole valence bands along the high-symmetry directions in momentum space for OP magnetization and IP magnetization with 3 times SOC strength. One can see that the nonzero Berry curvatures mainly localize around the Γ point. where the maximally localized Wannier functions[55–58] were constructed via non-self-consistent calculations on a $9 \times 9 \times 1$ k-point grid. Figures 6(a) and 6(e) display the band structure and Berry curvature distribution of OP magnetization and IP magnetization with 3 times SOC strength, showing that the band structure obtained from the Wannier interpolation scheme is essentially the same as that from the density functional theory (DFT) calculations. Moreover, the nontrivial Berry curvature was mainly distributed around the Γ point. By integrating the non-Abelian Berry curvature over the first BZ, we find that the Chern number (C) obtained is 1. Thus, the anomalous Hall conductivity shows a quantized charge Hall plateau at a value of $\sigma_{xy} = e^2/h$ located in the insulating gap of the spin-down Dirac cone, as shown in Figs. 6(d) and 6(h). Such a nonzero Chern number ($C = 1$) and quantized Hall conductivity character intrinsic QAH phase in this lattice. It is known that one of the remarkable features of topological materials is their robust edge states. To reveal the nontrivial topological nature of both systems, we calculate the local density of state (LDOS) of the edge states using Green's functions based on Wannier functions.[57,59] Figures 6(c) and 6(g) display the fitted DFT and TB bands as well as LDOS on the edge states. We find that the edge states connecting the valence and conduction bands cross the insulating gap of the spin-down channel, confirming their nontrivial topological nature. Remarkably, the spin texture of the edge state shows that the edge state is 100% spin-polarized in the z-direction, indicating half-metallic behavior. The half-metallic behavior obtained here is distinct from that of traditional half-metal for which spin-polarization may be highly suppressed upon consideration of SOC.

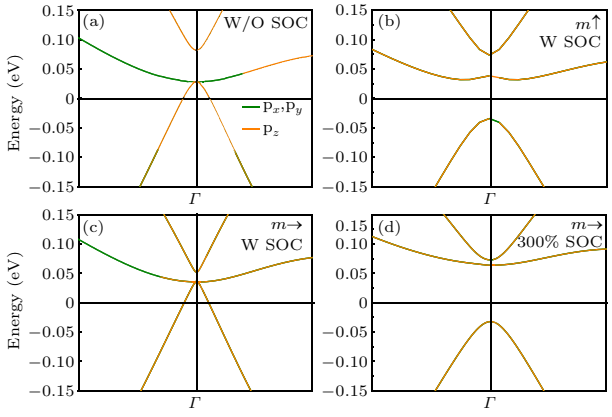


Fig. 5. (a)–(d) The projection of the bands in Figs. 4(b), 4(d), 4(f) and 4(h) onto atomic orbitals, including the N p_x/p_y orbital (green) and the N p_z orbital (orange).

In another primitive reciprocal lattice vector k_y, the hybrid Wannier charge centers (WCCs) can be defined as

$$\bar{x}_n(k_y) = \frac{\mathrm{i}}{2\pi}\int_{-\pi}^{\pi} \mathrm{d}k_x \left\langle u_n(k_x,k_y)\left|\partial k_x\right|u_n(k_x,k_y)\right\rangle, \quad (7)$$

where $u_n(k_x,k_y)$ is the periodic part of the Bloch function $\psi_n(k_x,k_y)$, Chern number C is defined as the change of the sum of hybrid WCCs $\bar{x}_n$ during a continuous deformation

$$C = \sum_n \bar{x}_n(2\pi) - \sum_n \bar{x}_n(0). \quad (8)$$

As can be seen from part IV of the ESI, which was calculated by Wannier-Tools, the electronic polarization WCCs shifts wards with the winding number 1, so the Chern number $|C| = 1$.

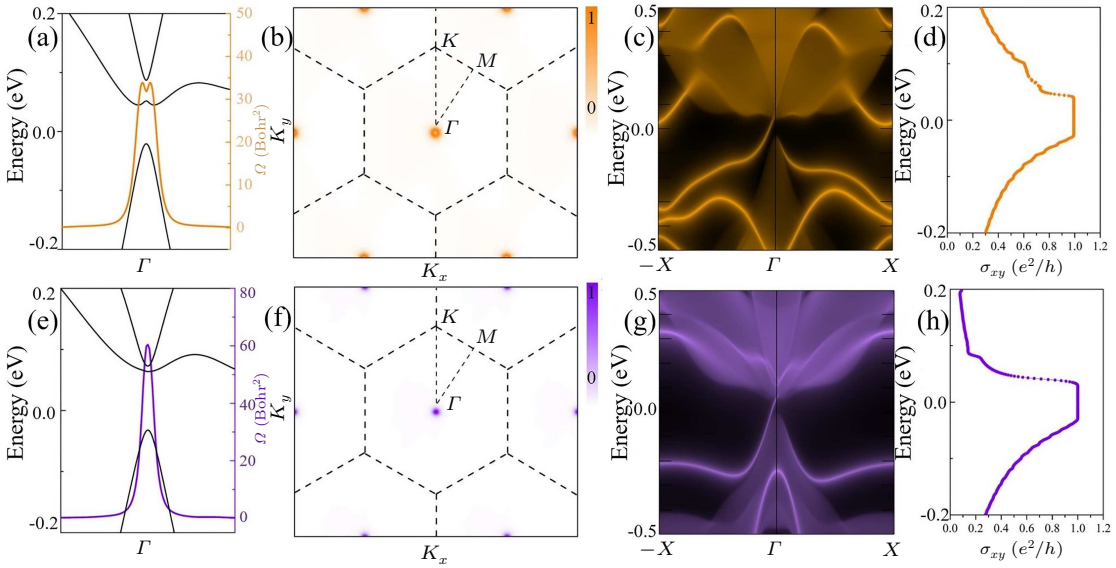


Fig. 6. (a) and (e) Band structures of PbN_2 with SOC along the z axis and band structures of PbN_2 with 3 times SOC along the x axis. The orange and purple dots denote the Berry curvature. (b) The Berry curvature along z axis and along x axis for the whole valence bands along high-symmetry directions in momentum space. (c) and (g) Calculated edge state. (d) and (h) Hall conductance of PbN_2.

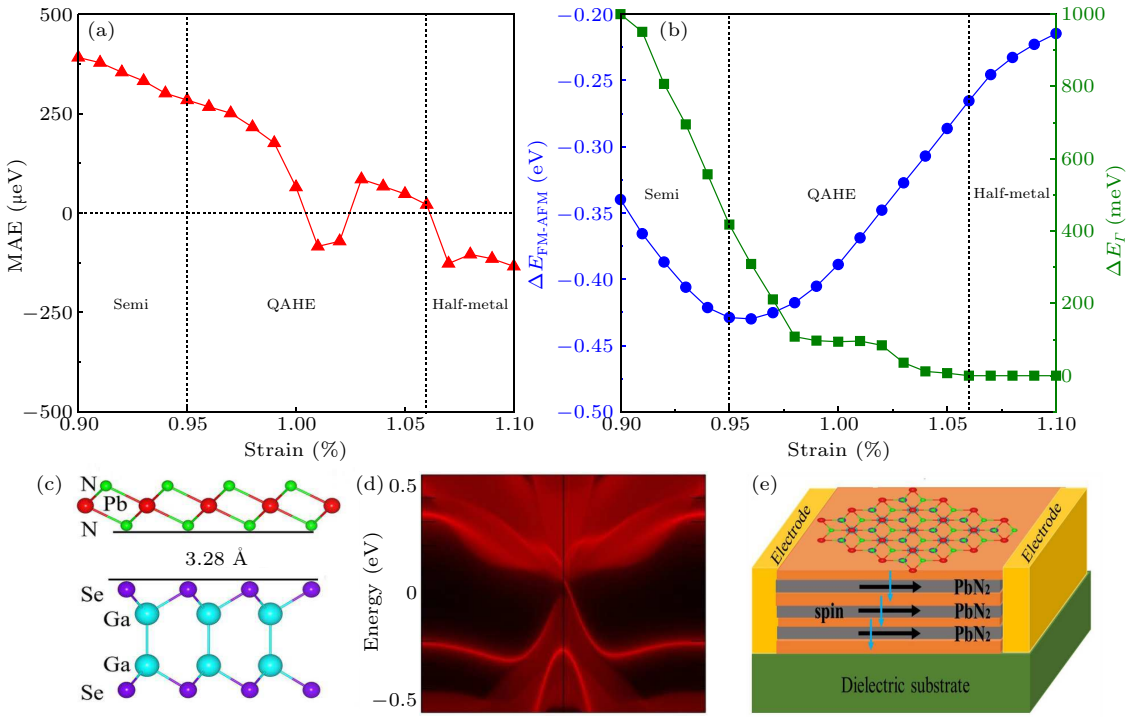


Fig. 7. (a) The evolution of topological phase and MAE phase for PbN_2 under different strains. (b) The variations of corresponding band gap E_Γ (green line) for PbN_2 and exchange energy (blue line) as a function of biaxial strains. (c) Side view of the epitaxial growth of the PbN_2/Ga_2Se_2 heterostructure. (d) The nontrivial topological edge states of the PbN_2/Ga_2Se_2 heterostructure. (e) Model of the topological field-transistor device. The PbN_2 monolayer is deposited on a dielectric substrate and sandwiched between two electrodes, which can drive net electric current conducting through the edge states in the sample. The fully spin-polarized currents are conducted through the topologically nontrivial half-metallic edge states. The red arrows indicate the spin direction, which is perpendicular to the sample plane.

To utilize a 2D crystal in device, it is essential to deposit it on a specific substrate, and, thus, inevitably relaxation strain is generated. Thus, the robustness of the QAHE against biaxial strains is investigated for the ML-PbN_2. Biaxal strain is applied by altering the lattice constant of the monolayer, i.e., $\varepsilon = (a - a_0)/a_0$, where a (a_0) is the strained (equilibrium) lattice constant. Figure 7(a) shows the variations of E_{MAE} and figure 7(b) shows the bulk gap (ΔE_Γ) at the Γ point and ΔE ($\Delta E = E_{FM} - E_{AFM}$) as well as the topological character with respect to strain ε. Notice that the FM ground state of the monolayer is maintained during the whole process of strain application. We find that nontrivial topology remains within the strain range of -5% to -6% for the PbN_2 monolayer. As the strain intensity increases, from -10% to 10%, the topological phase transition from normal insulator to QAH insulator to half-metal occurs. More interestingly, a larger gap of 0.51 eV is obtained under a tensile strain of -5% for PbN_2. In the light of the strain-modulated topological phase transition mentioned above, dissipationless, 100% spin-polarized, and high-speed electronic transport can be realized in a single device. Thus, we propose a new model of the topological field transistor (TFT) with a high 'ON–OFF' ratio engineered by external strains, as illustrated in Fig. 7(e). The currents in this device can flow across the edge region without applied strain, which is called the 'ON' state. When the applied compressive strain is beyond 5%, the normal insulator state appears with the conducting channel blocked and reflected back, resulting in an 'OFF' state. This principle provides an ideal platform for developing high-performance spintronic devices based on the QAH effect.

4. Conclusion

In summary, we proposed that the band inversion between $p_{x,y}$ and p_z orbitals could produce a topological phase transition in a honeycomb lattice based on sp^3 tight-binding (TB) model analyses. Based on first-principles calculations, two systems, i.e., 1T-XN_2 (X = Sn, Pb) were designed to realize the QAH effect, indicating that the underlying physical mechanism of our scheme is generally applicable. Spin-polarized band structures reveal that PbN_2 exhibits SGS character. When the spin and orbital degrees of freedom are allowed to couple, they result in a Chern insulator with large band gaps. Even in the case of in-plane magnetization, QAHE can be realized when SOC strength is large enough, and the SOC strength of a single layer can be regulated by doping different concentrations of Pt, Sb, Bi, and other metal atoms.[60–64] The band structure of Bi atom doping can be seen in part VII of the ESI. In particular, both systems could exhibit an intrinsic QAH effect even with a high Curie temperature of 768.7 K. When forming a PbN_2/Ga_2Se_2 heterostructure, the magnetization can alter within IP and OP directions. Our work offers broader opportunities for the exploration of novel topological states, especially when searching for high-temperature QAHE systems.

Acknowledgments

Project supported by Taishan Scholar Program of Shandong Province (Grant No. ts20190939), Independent Cultivation Program of Innovation Team of Jinan City (Grant No. 2021GXRC043), and the National Natural Science Foundation of China (Grant No. 52173283).

References

[1] Wang J, Li H, Chang C, *et al.* 2012 *Nano Research* **5** 739
[2] Qi X L and Zhang S C 2011 *Rev. Mod. Phys.* **83** 1057
[3] Bansil A, Lin H and Colloquium D T 2016 *Rev. Mod. Phys.* **88** 021004
[4] Liu P, Williams J R and Cha J J 2019 *Nat. Rev. Mater.* **4** 479
[5] Li X Y, Ji W X, Wang P J, *et al.* 2021 *Nanoscale Adv.* **3** 847
[6] Sun H, Li S S, Ji W X and Zhang C W 2022 *Phys. Rev. B* **105** 195112
[7] Li H, Chen C Z, Jiang H, *et al.* 2021 *Phys. Rev. Lett.* **127** 236402
[8] Liu C X, Qi X L, Dai X, *et al.* 2008 *Phys. Rev. Lett.* **101** 146802
[9] Zhang H, Lazo C, Blügel S, *et al.* 2012 *Phys. Rev. Lett.* **108** 056802
[10] You J Y, Chen C, Zhang Z, *et al.* 2019 *Phys. Rev. B* **100** 064408
[11] Zhang L, Zhang C W, Zhang S F, *et al.* 2019 *Nanoscale* **11** 5666
[12] Zhang S J, Zhang C W, Zhang S F, *et al.* 2017 *Phys. Rev. B* **96** 205433
[13] Wu S C, Shan G and Yan B 2014 *Phys. Rev. Lett.* **113** 256401
[14] Huang S M, Lee S T and Mou C Y 2014 *Phys. Rev. B* **89** 195444
[15] Li S S, Ji W X, Hu S J, *et al.* 2017 *ACS Appl. Mater. Inter* **9** 41443
[16] Ding J, Qiao Z, Feng W, *et al.* 2011 *Phys. Rev. B* **84** 195444
[17] Acosta C M, Lima M P, Miwa R H, *et al.* 2014 *Phys. Rev. B* **89** 155438
[18] Zhang M H, Zhang C W, Wang P J, *et al.* 2018 *Nanoscale* **10** 20226
[19] Zou R, Zhan F, Zheng B, *et al.* 2020 *Phys. Rev. B* **101** 161108
[20] Garrity K F and Vanderbilt D 2013 *Phys. Rev. Lett.* **110** 116802
[21] Wang Y P, Li S S, Zhang C W, *et al.* 2017 *Appl. Phys. Lett.* **110** 213101
[22] Wang Z F, Liu Z and Liu F 2013 *Phys. Rev. Lett.* **110** 196801
[23] Yu R, Zhang W, Zhang H J, *et al.* 2010 *Science* **329** 61
[24] Chang C Z, Zhang J, Feng X, *et al.* 2013 *Science* **340** 167
[25] Wu B, Song Y L, Ji W X, *et al.* 2023 *Phys. Rev. B* **107** 214419
[26] Liu C, Wang Y, Li H, *et al.* 2020 *Nat. Mater.* **19** 522
[27] Von Klitzing K 1986 *Rev. Mod. Phys.* **58** 519
[28] Liu X, Hsu H C and Liu C X 2013 *Phys. Rev. Lett.* **111** 086802
[29] Ren Y, Zeng J, Deng X, *et al.* 2016 *Phys. Rev. B* **94** 085411
[30] Zhong P, Ren Y, Han Y, *et al.* 2017 *Phys. Rev. B* **96** 241103
[31] Henk J, Flieger M, Maznichenko I V, *et al.* 2012 *Phys. Rev. Lett.* **109** 076801
[32] Liu Z, Zhao G, Liu B, *et al.* 2018 *Phys. Rev. Lett.* **121** 246401
[33] Zhao Y, Kamiya K, Hashimoto K, *et al.* 2015 *J. Am. Chem. Soc.* **137** 110
[34] Onodera M, Kawamura F, Cuong N T, *et al.* 2019 *APL Mater.* **7** 101103
[35] Kresse G and Furthmüller J 1996 *Phys. Rev. B* **54** 11169
[36] Perdew J P, Burke K and Ernzerhof M 1998 *Phys. Rev. Lett.* **80** 891
[37] Perdew J P, Burke K and Ernzerhof M 1996 *Phys. Rev. Lett.* **77** 3865
[38] Kresse G and Joubert D 1999 *Phys. Rev. B* **59** 1758
[39] Gonze X and Lee C 1997 *Phys. Rev. B* **55** 10355
[40] Togo A and Tanaka I 2015 *Scripta Mater.* **108** 1
[41] Bucher D, Pierce L C T, Mccammon J A, *et al.* 2011 *J. Chem. Theory Comput.* **7** 890
[42] Mostofi A A, Yates J R, Pizzi G, *et al.* 2014 *Comput. Phys. Commun.* **185** 2309
[43] Liu Y and Allen R E 1995 *Phys. Rev. B* **52** 1566
[44] Thouless D J, Kohmoto M, Nightingale M P, *et al.* 1982 *Phys. Rev. Lett.* **49** 405
[45] Yao Y, Kleinman L, Macdonald A H, *et al.* 2004 *Phys. Rev. Lett.* **92** 037204
[46] Skirlo S A, Lu L, Igarashi Y C, *et al.* 2015 *Phys. Rev. Lett.* **115** 253901
[47] Zhang K, Jin B J, Gao Y J, Zhang S, Shin H, Zeng H and Park J H 2019 *Small* **15** 1804903
[48] Yu Y J, Yang F Y, Lu X F, *et al.* 2015 *Nat. Nanotechnol.* **10** 270

[49] Sugawara K, Nakata Y, Shimizu R, *et al.* 2016 *ACS Nano* **10** 1341
[50] Li X R, Zhang Z Y and Zhang H B 2020 *Nanoscale Adv.* **2** 495
[51] Liu J Y, Liu Z F, Song T L, *et al.* 2017 *J. Mater. Chem. C* **5** 727
[52] Ertekin E, Chrzan D C and Daw M S 2009 *Phys. Rev. B* **79** 155421
[53] Liu J, Liu Z, Song T, *et al.* 2017 *J. Mater. Chem. C* **5** 727
[54] Codello A and D'odorico G O 2013 *Phys. Rev. Lett.* **110** 141601
[55] Halilov S V, Perlov A Y, Oppeneer P M, *et al.* 1998 *Phys. Rev. B* **57** 9557
[56] Kou X, Guo S T, Fan Y, *et al.* 2014 *Phys. Rev. Lett.* **113** 137201
[57] Marzari N and Vanderbilt D 1997 *Phys. Rev. B* **56** 12847
[58] Souza I, Marzari N and Vanderbilt D 2001 *Phys. Rev. B* **65** 035109
[59] Mostofi A A, Yates J R, Lee Y S, *et al.* 2008 *Comput. Phys. Commun.* **178** 685
[60] Zhao H, Zhang C W, Ji W X, *et al.* 2016 *Sci. Rep.* **6** 1
[61] Zhang R W, Ji W X, Zhang C W, *et al.* 2016 *J. Mater. Chem. C* **4** 2088
[62] Lee Y, Eu P, Lim C Y, *et al.* 2021 *Current Appl. Phys.* **30** 4
[63] Cho S W, Lee M, Woo S, *et al.* 2018 *Sci. Rep.* **8** 5739
[64] Zhu L, Ralph D C and Buhrman R A 2019 *Phys. Rev. Lett.* **122** 077201